ACS NANO

www.acsnano.org

ARTICLE

Room Temperature Magnetic Skyrmions in Gradient-Composition Engineered CoPt Single Layers

Adam Erickson,[†] Qihan Zhang,[†] Hamed Vakili,[†] Chaozhong Li, Suchit Sarin, Suvechhya Lamichhane, Lanxin Jia, Ilja Fescenko, Edward Schwartz, Sy-Hwang Liou, Jeffrey E. Shield, Guozhi Chai, Alexey A. Kovalev, Jingsheng Chen,* and Abdelghani Laraoui*

Cite This: *ACS Nano* 2024, 18, 31261−31273

Read Online

ACCESS | Metrics & More | Article Recommendations | Supporting Information

ABSTRACT: **Topologically protected magnetic skyrmions in magnetic materials are stabilized by an interfacial or bulk Dzyaloshinskii−Moriya interaction (DMI). Interfacial DMI decays with an increase of the magnetic layer thickness in just a few nanometers, and bulk DMI typically stabilizes magnetic skyrmions at low temperatures. Consequently, more flexibility in the manipulation of DMI is required for utilizing nanoscale skyrmions in energy-efficient memory and logic devices at room temperature (RT). Here, we demonstrate the observation of RT skyrmions stabilized by gradient DMI (g-DMI) in composition gradient-engineered CoPt single-layer films by employing the topological Hall effect, magnetic force microscopy, and nitrogen-vacancy scanning magnetometry. Skyrmions remain stable over a wide range of applied magnetic fields and are confirmed to be nearly Bloch-type from micromagnetic simulation and analytical magnetization reconstruction. Furthermore, we observe skyrmion pairs, which may be explained by skyrmion−antiskyrmion interactions. Our findings expand the family of magnetic materials hosting RT magnetic skyrmions by tuning g-DMI via gradient polarity and a choice of magnetic elements.**

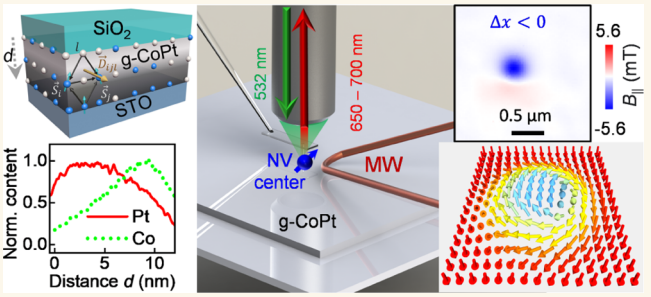

KEYWORDS: *skyrmion, topological stability, Dzyaloshinskii−Moriya interaction, topological Hall effect, nitrogen vacancy, CoPt*

Magnetic skyrmions are topologically nontrivial vortex-like quasiparticles that possess nano- to microscale dimensions and high controllability through current-induced spin torque.[1] When stabilized at room temperature (RT), they could be used as memory and logic elements promising for next-generation energy-efficient memory and logic devices[2] as well as neuromorphic computing.[3,4] Dzyaloshinskii−Moriya interaction (DMI) is an indirect and antisymmetric exchange interaction favoring the formation of magnetic skyrmions. Néel skyrmions, Bloch skyrmions, and antiskyrmions have been experimentally observed in various materials. In ultrathin ferromagnetic/heavy metal (FM/HM) multilayers, interfacial DMI[5−7] originates from broken inversion symmetry at interfaces between the FM and HM layers with strong spin−orbit coupling (SOC).[1] In this case, Néel-type skyrmions have been identified not only in monolayer Fe/Ir(111) and bilayer PdFe/Ir(111)[8,9] but also in several FM/HM heterostructures composed of subnanometer Co layers sandwiched between HM layers (Ir, Pt, W).[7,10−12] Examples include $[Ir/Co/Pt]_{10}$ multilayer structures.[10] However, interfacial DMI strength in FM/HM multilayer systems vanishes by increasing the thickness of the FM layer to a few nanometers, and the stability of the magnetic skyrmions relies heavily on the quality of interfaces. In contrast, bulk DMI-induced Bloch-type skyrmions in chiral magnet B20-type compounds such as MnSi,[13] $Fe_{1-x}Co_xSi$,[14] and FeGe were observed at low temperatures.[15,16] Recently, RT skyrmions were observed in chiral magnet $Co_8Zn_{10}Mn_2$ that can be manipulated electrically.[17,18] However, materials with bulk DMI are rare, and the DMI strength lacks tunability since it is set by the crystal structure. Furthermore, antiskyrmions, characterized by the opposite winding number and anisotropic helicity, can be stabilized at RT by anisotropic DMI[19] in Heusler compounds

Received: July 26, 2024
Revised: October 13, 2024
Accepted: October 18, 2024
Published: October 29, 2024

https://doi.org/10.1021/acsnano.4c10145
ACS Nano 2024, 18, 31261−31273

$Mn_{1.4}PtSn$[20,21] and $Mn_{1.4}Pt_{0.9}Pd_{0.1}Sn$.[22,23] Skyrmion−antiskyrmion pairs were also observed in B20-type FeGe.[16]

Very recently, sizable DMI was realized at RT by a compositional gradient engineering in single-layer films consisting of FM and HM, referred to as gradient DMI (g-DMI). The resulting g-DMI originates from the combined bulk magnetization asymmetry (BMA) and SOC, and has sign and strength dependence with the magnetization gradient.[24,25] Although it is believed that magnetic skyrmions could be stabilized by g-DMI, direct observation of spin textures in gradient samples is still missing. In addition to g-DMI, nonequilibrium spin torque could originate from the composition gradient-induced symmetry breaking. In particular, field-free spin−orbit torque induced magnetization self-switching is reported in gradient CoTb[26] and CoPt[27] single layers. Magnetic skyrmions combined with spin torque extend the application of gradient magnetic single-layer systems to spintronics. Motivated by these findings, we have investigated the presence of topological spin textures in gradient CoPt alloy single-layers through direct magnetic imaging.

Here, we use scanning nitrogen-vacancy (NV) magnetometry in combination with magnetic force microscopy (MFM), Brillouin light scattering (BLS), and the topological Hall effect (THE) to observe RT magnetic skyrmions in composition gradient engineered CoPt single layers. Isolated skyrmions are measured by MFM and found to correlate to the field-dependent topological Hall signal, indicating nonzero topology. Micromagnetic simulation and analytical magnetization reconstructions extracted from NV magnetic stray-field maps reveal nearly Bloch-type skyrmions. The isolated skyrmions remain stable over a wide range of applied magnetic fields. Pairs of skyrmions were also observed, which may be attributed to higher-order winding number skyrmions, trivial skyrmions, or by skyrmion−antiskyrmion interaction. Of particular interest is observing/controlling exotic topologically protected spin textures in composition gradient magnetic single-layer systems and greatly expanding the selection range of materials for the research and application of magnetic skyrmions.[1]

RESULTS AND DISCUSSION

Structural and Magnetic Properties of CoPt Single Layer with Gradient. To host topological spin textures, DMI was introduced into binary Co_xPt_{1-x} films with perpendicular magnetic anisotropy (PMA) via a composition gradient-induced bulk inversion asymmetry.[24,27] In the framework of the three-site Fert−Lévy model, the net bulk DMI is stabilized due to the compositional gradient of FM/HM single layer shown in Figure 1a, where an antisymmetric exchange interaction between neighboring FM (blue spheres) atoms (sites i and j) is enabled by the SOC of the HM (gray spheres) atom (site l) via conduction electrons. The DMI vector is given by the formula[28]

$$\vec{D}_{ijl}(\vec{R}_{li},\vec{R}_{lj},\vec{R}_{ij}) = -V_1\frac{(\vec{R}_{li}\times\vec{R}_{lj})(\vec{R}_{li}\times\vec{R}_{lj})}{|\vec{R}_{li}|^3|\vec{R}_{lj}|^3|\vec{R}_{ij}|} \quad (1)$$

where $|\vec{R}_{li}|$, $|\vec{R}_{lj}|$, and $|\vec{R}_{ij}|$ are the distance vectors and V_1 is the SOC material parameter.[25]

The starting and ending components of Co_xPt_{1-x} defined as $Co_{x_i}Pt_{1-x_i}$ and $Co_{x_t}Pt_{1-x_t}$ give the value of gradient $\Delta x = x_t - x_i$, wherein, $x_i(x_t)$ represents the starting (ending) stoichiometric ratio of Co. 10 nm-thick Co_xPt_{1-x} single layer films with positive ($\Delta x = +50\%$) and negative ($\Delta x = -50\%$) composition gradient were synthesized using a cosputtering technique (see Methods), which is similar to that used in ref 25. The corresponding composition from start to end is $CoPt_3 \rightarrow Co_3Pt$ ($Co_3Pt \rightarrow CoPt_3$) for positive gradient $\Delta x = +50\%$ (negative gradient $\Delta x = -50\%$). In the following, we refer to gradient Co_xPt_{1-x} single layers as g-CoPt. The smooth surfaces were confirmed through atomic force microscopy (AFM) topography measurements; see the Supporting Information (SI), Section S1 and Figure S1.1. The high-resolution X-ray diffraction (HR-XRD) patterns were measured on both $\Delta x = -50\%$ and $\Delta x = +50\%$ g-CoPt films shown in Figure 1b. The (111) diffraction peaks of g-CoPt films with $\Delta x = -50\%$ and $\Delta x = +50\%$ were observed around 42°. The broadening of diffraction peaks may stem from the contribution of Co_xPt_{1-x} having different compositions. It is noted that the (111) peak of homogeneous Co_xPt_{1-x} crystal shifts toward a higher position with the increase of x, owing to the smaller atomic size of Co than that of Pt (see SI Figure S1.2).

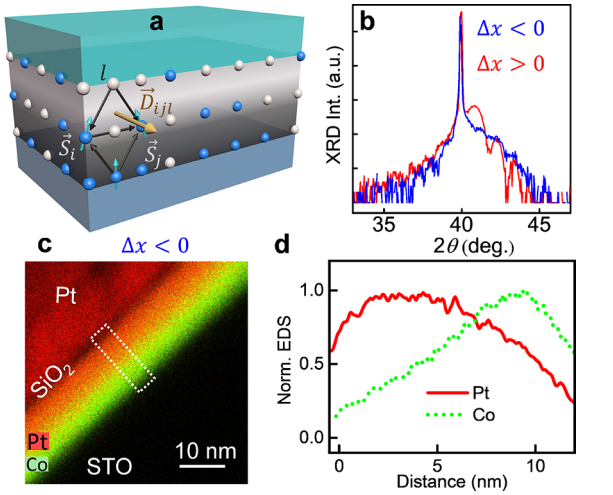

Figure 1. Structural characterization of g-CoPt single layer with g-DMI. (a) Schematic of the bulk DMI arising in FM/HM film from the combination of BMA induced by composition gradient and strong SOC in HM. The induced DMI vector $\vec{D}_{ijl}$ can be described by the three site Fert-Lévy model, with magnetic atoms ($\vec{S}_i$, $\vec{S}_j$) and heavy metal atom (l) participating in asymmetric exchange interaction. (b) XRD spectrum for $\Delta x = -50\%$ (blue) and $\Delta x = +50\%$ (red) g-CoPt single layers. (c) STEM-EDS image of $\Delta x = -50\%$ g-CoPt with plotted contribution of Co (green) and Pt (red). (d) Normalized EDS intensity for Pt (red solid line) and Co (dotted green line) for $\Delta x = -50\%$ g-CoPt, integrated across the dashed rectangle in (c).

Energy dispersive X-ray spectroscopy (EDS) in a scanning transmission electron microscopy (STEM) configuration was used to map the compositional aspects of the $\Delta x = -50\%$ g-CoPt single layer. The EDS compositional map shown in Figure 1c reveals the presence of Co and Pt through the gradient film thickness. It should be noted that the Pt region in the upper left portion of the image is the Pt layer deposited to protect the CoPt film from any damage from Ga ions during STEM sample preparation using standard lift-out techniques.[29] The thin SiO_2 layer delineates the protective Pt layer from the film. The relative Co and Pt contents in the film (Figure 1d) show the evolution of the composition through the thickness

https://doi.org/10.1021/acsnano.4c10145
ACS Nano 2024, 18, 31261−31273

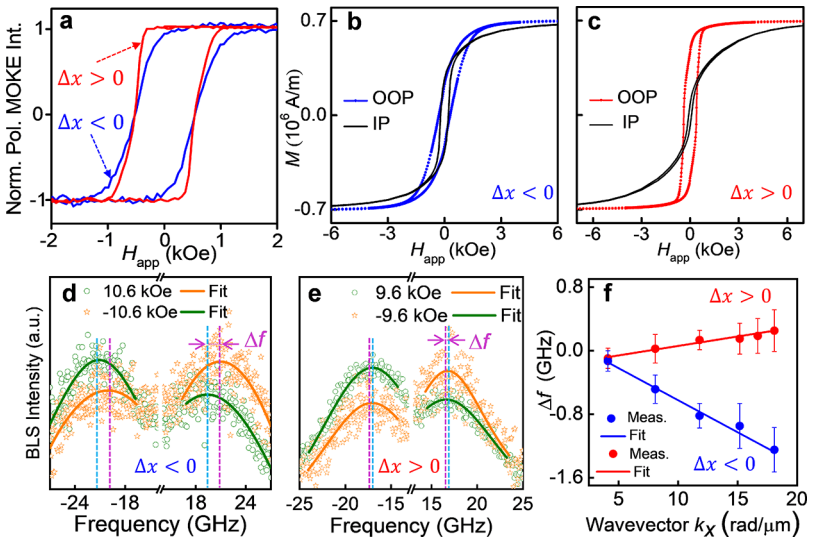

Figure 2. Magnetic characterization of the g-CoPt single layer with g-DMI. (a) Normalized MOKE intensity vs applied magnetic field for Δx = −50% and Δx = +50% g-CoPt films. OOP (scattered lines) and IP (solid lines) $M-H$ hysteresis loops of g-CoPt films with compositional gradient Δx = −50% (b) and Δx = +50% (c). BLS spectra for Δx = −50% (d) and Δx = +50% (e) g-CoPt films in which the scattered green and orange curves represent the spectra with $\pm \mu_0 H$ and the solid lines are the fitting curves. (f) Δf vs k_x for g-CoPt (Δx = ± 50%) films.

of the film. This was obtained by quantifying the individually normalized Co and Pt contents within the dashed area shown in Figure 1c. For most of the film, the relative EDS signal is linearly varying, suggesting that the magnetization is distributed asymmetrically.

To quantify the magnetism of g-CoPt films, magneto-optical Kerr effect (MOKE), superconducting quantum interference device (SQUID) magnetometry, and BLS spectroscopy were used. Figure 2a shows the normalized polar MOKE signal intensity as a function of the applied magnetic field H_{app} for g-CoPt (Δx = −50%) and g-CoPt (Δx = +50%) films, demonstrating a difference of PMA. $M-H$ hysteresis loops measurements with out-of-plane (OOP) and in-plane (IP) applied magnetic fields were conducted by SQUID magnetometry (Methods). Figure 2b,c shows the $M-H$ hysteresis loops measured in g-CoPt films with Δx = −50% and Δx = +50%. The corresponding saturation magnetization (M_s) and effective perpendicular magnetic anisotropy constant (K_{eff}) could be obtained: similar M_s values of 717 kA/m for both films, K_{eff} = 0.384 mJ/m^2 and 1.11 mJ/m^2 for g-CoPt (Δx = −50%) and g-CoPt (Δx = +50%) films, respectively. The contrast of K_{eff} between negative and positive g-CoPt films may originate from the influence of crystallographic degree under different stacking orders (see SI Section S1).

It is predicted that BLS spectroscopy is a powerful technique to quantify DMI. Both the amplitude and sign of DMI could be determined by measuring the nonreciprocal frequency shift of Damon−Eshbach (DE) spin waves.[30−33] The frequency shift Δf between the counterpropagating DE spin waves ($\pm k_x$) induced by DMI is given by

$$\Delta f = f_{DM}(-k_x, M_z) - f_{DM}(k_x, M_z) = \frac{2\gamma}{\pi M_s} D k_x \quad (2)$$

where γ, M_s, D, and k_x are the gyromagnetic ratio, the saturation magnetization, the volume-averaged DMI constant, and the projection of the spin-wave vector ($\boldsymbol{k}$) in the direction perpendicular to the applied magnetic field $\mu_0 H$, respectively. Figure 2d,e shows the typical BLS spectra for g-CoPt (Δx = ± 50%) films with k_x = 18.09 rad/μm, in which a positive (negative) frequency shift corresponds to the film with a positive (negative) gradient. The evolution of Δf vs k_x for g-CoPt (Δx = ± 50%) films is summarized in Figure 2f. The opposite slope of Δf vs k_x suggests that a positive (negative) magnetization gradient gives rise to positive (negative) DMI. Through the linear fitting, the volume-averaged DMI constants D could be obtained: 0.15 mJ/m^2 for g-CoPt (Δx = +50%) films and −0.51 mJ/m^2 for g-CoPt (Δx = −50%) films. The difference in DMI amplitude in g-CoPt (Δx = ± 50%) films is observed to which the additional long-range asymmetries along the thickness direction may also contribute.

Magneto-Transport and MFM Characterization of g-CoPt Single Layers. The magnetic field dependent spin textures are studied on the positive and negative g-CoPt (Δx = ± 50%) films. As electrons pass through magnetic skyrmions, an additional THE signal contributes to the Hall resistance. The relationship between THE signal and magnetic textures with the change of magnetic field could be a fingerprint for the presence of skyrmions.[34] The g-CoPt films were fabricated (Methods) into Hall bar devices for transport measurement. Then, the Hall resistance ρ_{xy} was measured with a swept OOP magnetic field H_{app}. The contribution of longitudinal resistivity could be excluded due to the disappearance of anisotropic magnetoresistance and large length-width ratio. To extract the THE signal $\rho_{TH}(H_{app})$,[34] the residual resistivity $\Delta\rho_{xy}(H_{app})$ is estimated through the fit of $\rho_{xy}(H_{app})$ to $\rho_{xy}^{fit}(H_{app}) = R_0 H_{app} + R_s M(H_{app})$ (see SI Section S2). The magnetic hysteresis loops $M(H_{app})$ for both Δx = −50% and Δx = +50% g-CoPt single layers were measured by SQUID (see Figure 3a and Figure S2a). The presence of nonzero $\Delta\rho_{xy}(H_{app})$ is also confirmed when measured by MOKE (Figure 2a), which is collected in the center of the Hall bar (see the inset of Figure 3a). The features of the residual signal $\Delta\rho_{xy}(H_{app})$ between $\rho_{xy}(H_{app})$ and $\rho_{xy}^{fit}(H_{app})$ track the accumulation of the additional Berry phase contributed by the itinerant electrons interacting with topological spin textures (e.g., skyrmions).[34]

MFM was used to investigate the magnetic domain structure morphology associated with the THE signal $\Delta\rho_{xy}(H_{app})$ in Figure 3a, performed on g-CoPt (Δx = −50%) film. The

https://doi.org/10.1021/acsnano.4c10145
ACS Nano 2024, 18, 31261−31273

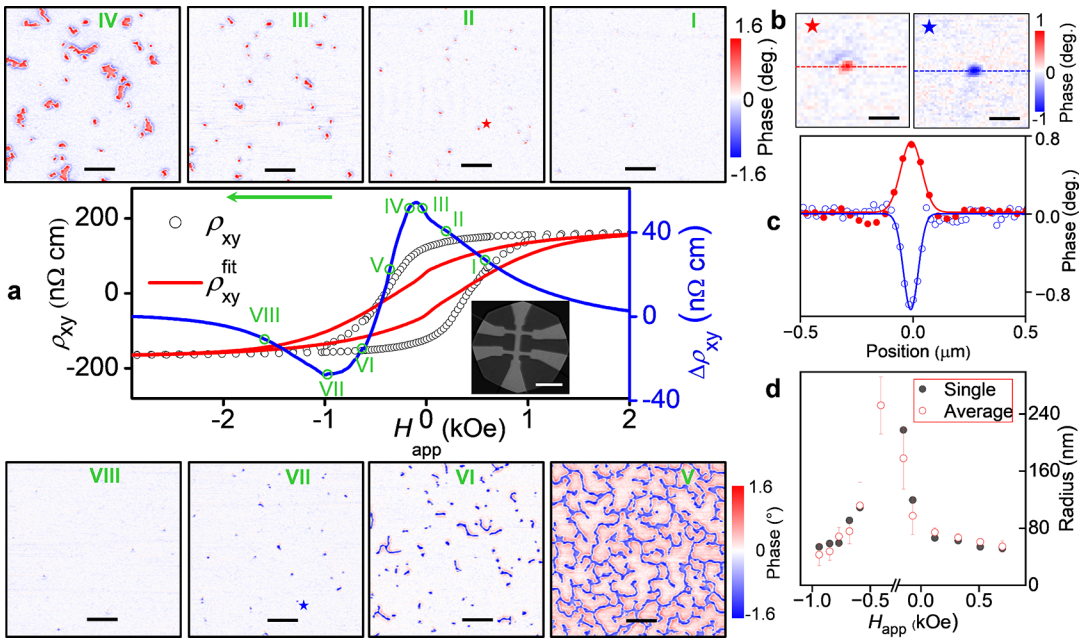

Figure 3. THE and MFM imaging of magnetic morphology through magnetic field sweep in g-CoPt (Δx= −50%) single layer. (a) THE curve (blue line) obtained by subtracting the fitting curve ρ_{xy}^{fit} (red line) from the Hall resistance curve (open circles). Inset of (a): Hall device (scale bar is 50 μm). (I−VIII) Selected MFM images under different magnetic fields are indicated by hollow green circles plotted on the THE curve. The scale bar in images I through VIII is 2 μm. (b) MFM images of individual skyrmions (denoted by red and blue stars in images II and VII, respectively) with color coded cross sections (circles) and Gaussian profile fitting (solid lines) in (c). (d) Comprehensive radius versus H_{app} obtained from MFM images, in which solid black circles (hollow red circles) represent single skyrmion radius (mean radius).

applied magnetic field H_{app} is swept from positive to negative saturation with MFM scans being acquired at intervals throughout the sweep (Figure 3a, I−VIII). Initially, in the magnetic field point (I), MFM displays mostly noise level signals with small features, corresponding to the nucleation of skyrmions, correlating with the initial increase in $\Delta\rho_{xy}(H_{app})$. At magnetic field points (II−V), there is a continuation of the nucleated skyrmion structures with a decreasing applied magnetic field until the domain structure begins to collapse into the spiral phase, and a more rapid magnetization reversal process takes place. This is reflected in the subsequent increase, maximum, and decrease in the THE signal. As the increasingly negative magnetic field is applied, we observe a somewhat symmetric behavior of about −0.3 kOe in both the THE and MFM images (VI−VIII), and the THE signal approaches zero as the film approaches the FM phase. Interestingly, there is even the preservation of certain domain positions after passing through the coercive equilibrium, likely associated with pinning centers. A similar comparison between MFM and THE in g-CoPt (Δx = +50%) film is shown and discussed in the SI, Section S2.

Details of isolated skyrmions containing opposite core magnetization are shown in Figure 3b. The reversal of the magnetic force interaction (opposite phase) from oppositely magnetized skyrmions indicates the preservation of MFM probe magnetization throughout the duration of the applied magnetic field sweep. Information about high coercivity, low moment MFM tips can be found in Methods and ref 35. Line-cuts of the isolated skyrmion profiles are fitted by Gaussian functions (Figure 3c). The extracted radius is then plotted versus the applied magnetic field H_{app} (Figure 3d), showing both the average behavior and the selected single skyrmion radius. In cases where the shape of isolated skyrmions deviated significantly from radial isotropy, thresholding techniques were employed, and the mean radius of the amorphous area was measured. The error bar represents the interquartile range of the measured skyrmion radii. It is worth noting that the full width at half-maximum (fwhm) of the Gaussian profile measured by MFM in Figure 3c is still a convolved signal and would require another level of analysis to estimate the radius defined by the underlying magnetization structure of the skyrmion. Furthermore, MFM images are inherently subject to the distortion caused by the back action of the magnetic field produced by the tip on the sample domain structure.[34,36] This is especially problematic in cases where the film has a high PMA, where the attractive magnetic field from the tip can more easily cause premature magnetization reversal. This effect was seen when imaging the 10 nm-thick g-CoPt (Δx = +50%) single layer, preventing the full comparison between THE and MFM (see Figure S2 in SI Section S2). MFM was also performed on the homogeneous Co_3Pt and $CoPt_3$ films as shown in Figure S1.3. The lack of observed spin textures in the ungraded samples is an indication that the magnetization gradient is integral to the stabilization of topological spin textures. This correlates well with BLS measurements of close to zero DMI in both Co_3Pt and $CoPt_3$ films, discussed in SI Section S1 and Figure S1.4.

Vector Magnetometry of Isolated Skyrmions. Recently, another technique has emerged for measuring magnetic fields at the nanometer scale without interfering with magnetic samples based on optical detection of the electron spin resonances of NV centers in diamond.[37−43] Negatively charged NV centers, composed of a substitutional nitrogen adjacent to a vacancy site (Figure 4a), are bright, stable single photon emitters that exhibit high-contrast optical detected magnetic resonance (ODMR).[44] NV scanning probe microscopy (NV-

https://doi.org/10.1021/acsnano.4c10145
ACS Nano 2024, 18, 31261−31273

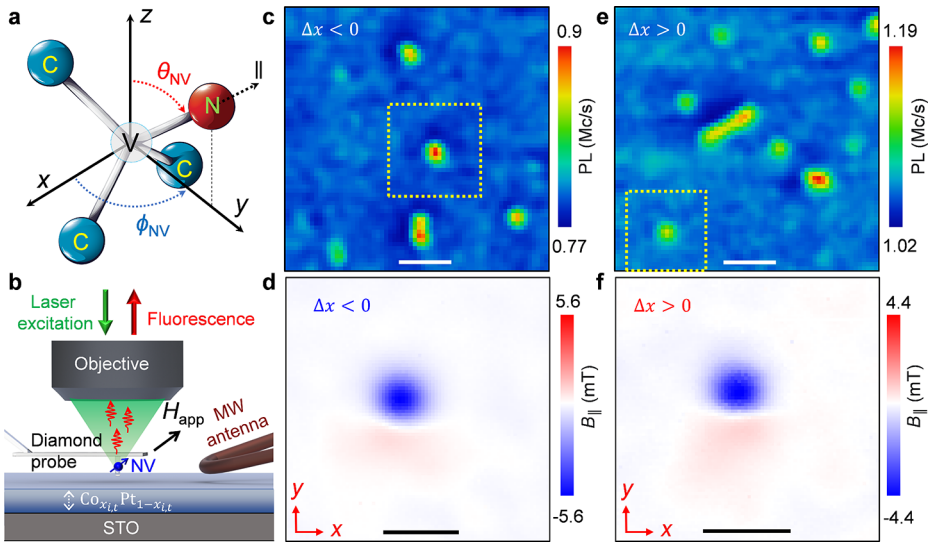

Figure 4. NV-SPM imaging of spin textures in g-CoPt single layer. (a) Sketch of the NV molecular structure in the diamond lattice, showing the NV sensing axis parallel (‖) to the applied magnetic field H_{app} relative to the Cartesian reference frame (x, y, z). (b) Schematic of the NV-SPM imaging apparatus, showing a high NA (0.7) objective used to focus a green (532 nm) laser on the diamond probe with single NV in the confocal geometry. NV PL images of skyrmions in g-CoPt film with compositional gradients Δx = −50% (c) and Δx = +50% (e), respectively. The scale bar in panels (c) and (e) is 1 μm. The NV standoff, d_{NV}, is 150 nm. (d, f) Two-dimensional $B_{\parallel}$ magnetic image for the skyrmions denoted by their scan area (yellow dashed square) in panels (c) and (e). NV standoffs are 230 and 200 nm in panels (d) and (f), respectively. The scale bar in panels (d) and (f) is 500 nm.

SPM) has been widely used to quantitatively measure static and dynamic magnetic stray fields of solid-state systems with a good combination of spatial resolution and magnetic sensitivity in a wide range of temperatures (0.3−600 K).[45−51] In particular, NV-SPM was used recently to image skyrmions in Co/Pt multilayers,[52,53] CoFeB thin films,[54] and Heusler alloys.[55]

In order to gain quantitative insight into the magnetization configurations of the positive and negative gradient composition g-CoPt films, we used NV-SPM (Figure 4b, see Methods and SI Section S3 for further details).[49,56,57] The orientation of the NV atomic structure with respect to the Cartesian reference frame is schematized in Figure 4a, indicating polar (θ_{NV}) and azimuthal (ϕ_{NV}) angles of 53 and 90°, respectively.[58] An external magnetic field H_{app} is applied along the NV symmetry axis to break the degeneracy of the m_S = ±1 state, creating a pair of spin transitions whose frequencies depend on the amplitude of H_{app}.[42,49,57] In addition, the distance between the NV and the g-CoPt surface, d_{NV}, is set to find a suitable measurement height, which optimizes the spatial resolution without degradation of the ODMR contrast due to spin mixing caused by the strong transverse magnetic stray field components.[59]

Initially, a rapid assessment of the spin textures is obtained using NV photoluminescence (PL) quenching imaging,[48] in which the strong stray field produced by the skyrmions can be read out through its encoded PL signal. PL quenching images of a g-CoPt single layer with compositional gradient Δx = −50% (Figure 4c) and Δx = +50% (Figure 4e) are obtained at H_{app} of 0.1 kOe. This method allows for a detailed map of the size and position of skyrmions in a static domain configuration, as demonstrated in $[Pt/Co/Ru]_{\times 2}$ multilayer stack.[48] Further discretion between the strength regimes of the magnetic stray field can be inferred by the distinction between positive (enhancement) and negative (quenching) photodynamics,[59] see SI Section S6.

Once suitably isolated skyrmions are located, ODMR imaging is performed to measure the parallel component of the stray field, $B_{\parallel}$, generated by the skyrmions at a distance d_{NV} above the magnetic sample. This distance is chosen based on the size of the skyrmion, which affects the resulting stray field magnitude.[52] The Hamiltonian of the system in the Cartesian lab coordinates (x, y, z) in Figure 4a is[44]

$$H = DS_z^2 - \gamma_{NV}(S_x(H_{app,x} + B_x) + S_y(H_{app,y} + B_y) + S_z(H_{app,z} + B_z)) \quad (3)$$

where γ_{NV} = 28 GHz/T is the gyromagnetic ratio of the electron spin, B_x, B_y, and B_z are the projections of the stray-field vector $\boldsymbol{B}$ along x, y, and z axes, respectively. By considering a linear dependence of the components of $B_{\parallel}$ in the Fourier space (see SI Section S5), one can use the upward propagation protocol to reconstruct the two-dimensional (2D) maps of B_z, B_x, and B_y at any height above the measurement plane from only one NV measurement of $B_{\parallel}$.[40,49,57] ODMR images for the isolated skyrmions highlighted in the PL maps in Figure 4c,e are shown in Figure 4d,f, obtained on compositional gradients of −50% and +50% g-CoPt, respectively.

Taking the results of g-CoPt (Δx = −50%) film for example, Figure 5b shows the simulated 2D $B_{\parallel}$ stray field of an isolated skyrmion (radius of 120 nm) compared with the measured one (Figure 5a), in which the resulting stray field is calculated by the NV parameters (d_{NV} = 320 nm, θ_{NV} = 53°, ϕ_{NV} = 90°) and the material parameters corresponding to calibration measurements (M_s = 700 kA/m, K_u = 420 kJ/m^3) are employed. The value of g-DMI measured by BLS for Δx = −50% g-CoPt of −0.5 mJ/m^2 was implemented in micromagnetic simulations as a uniform distribution through the thickness of the film, a property of g-DMI which was predicted from atomistic simulations.[24,25] Note that interfacial contribution can induce nonuniformity of total DMI; however, we do not observe any

https://doi.org/10.1021/acsnano.4c10145
ACS Nano 2024, 18, 31261−31273

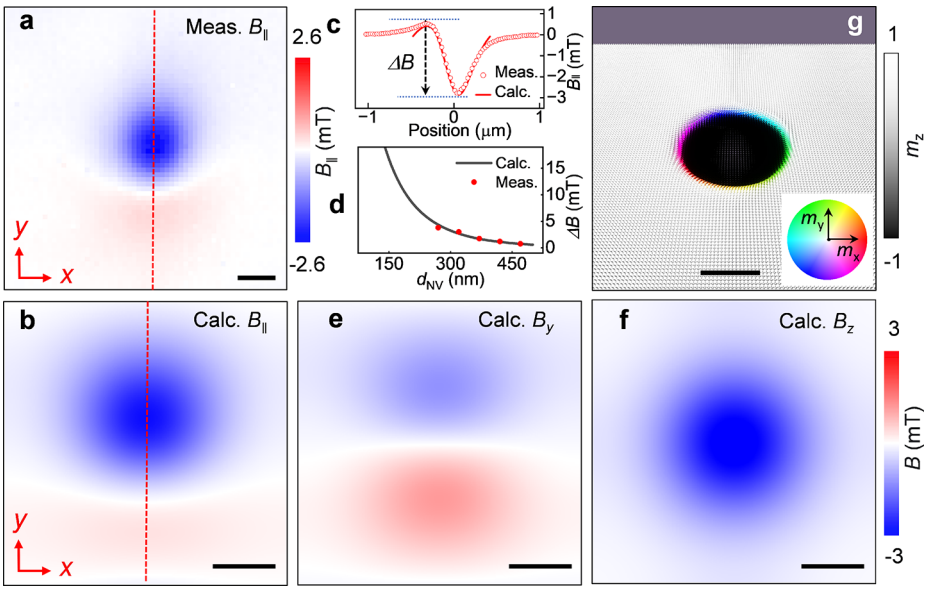

Figure 5. Micromagnetic simulation of isolated skyrmion in g-CoPt (Δx= −50%) single layer. Measured (a) and calculated (b) ODMR $B_\parallel$ image of a single skyrmion from g-CoPt single layer with compositional gradient Δx = −50% at an NV standoff d_{NV} of 320 nm and H_{app} of 0.23 kOe. (c) Extracted line profiles from measured (open circles) and simulated (solid line) skyrmion patterns in patterns (a) and (b), respectively. (d) Skyrmion pattern amplitude ΔB as a function of d_{NV} of measured (filled circles) and calculated (solid line) profiles in panel (c). (e, f) Projections of the stray field at 320 nm above the film surface along the NV sensing axes y and z, respectively. The scale bar in panels (a), (b), (e), and (f) is 200 nm. (g) Vectorial representation of hybrid skyrmion magnetization. The scale bar in panel (g) is 100 nm.

impact of such variation due to the small thickness of the g-CoPt films. The extracted line profiles from both measured (Figure 5a) and simulated (Figure 5b) $B_\parallel$ images are plotted in Figure 5c. Of note, the magnetic pattern amplitude ΔB can be calculated by subtracting the maximum and minimum values of $B_\parallel$.[43] Figure 5d displays ΔB as a function of d_{NV} in the range of 150 to 500 nm, deduced from NV measurement (filled circles) and micromagnetic simulation (solid line) $B_\parallel$ images. There is good agreement between the measured and simulated ΔB obtained values in the d_{NV} range of 200−470 nm. Below 200 nm, the magnetic stray field produced by the skyrmion is higher than the amplitude of H_{app}, which leads to a misalignment of the effective magnetic field (H_{app} + $B_\parallel$) along the NV axis, and a decrease in the NV ODMR contrast.[59] This is clearly seen in the NV PL imaging for d_{NV} < 100 nm where a sharp decrease in PL is observed (see SI Section S6), explained by the level mixing of NV spin transitions in the excited state induced by the high values of $B_\parallel$ (∼50 mT)[59] produced by the skyrmions. The calculated 2D maps of B_y (Figure 5e) and B_z (Figure 5f) are demonstrated to gain information about the vector representation of the skyrmion stray field. Figure 5g shows the simulated spin configuration of the skyrmion vectorially, predicting the hybrid-type spin texture with a helicity of around $\pi/4$ for stronger DMI.

Helicity and polarity are usually used to describe magnetic skyrmions.[60,61] Helicity is defined as the angle of the global rotation around the z-axis. Note that the helicity is $\pi/2$ (zero) for Bloch (Néel) skyrmions. Polarity describes whether the magnetization points in the positive (p = 1) or negative (p = −1) z direction at the center of the skyrmion. For Bloch and Néel skyrmions, the topological charge and polarity are equal (Q = p). Therefore, the difference in helicity distinguishes Bloch and Néel skyrmions from one another. To determine the helicity of the measured skyrmions in g-CoPt single layers, we systematically deduce the phase diagrams from simulations as a function of DMI strength and H_{app} (see SI Section S8, Figure S8.2) and found that skyrmions stabilize with a helicity that is determined by the competition between DMI and the dipolar interactions. For lower values of DMI, the near Bloch type helicity is stabilized.

Along with micromagnetic simulations, analytical reconstruction methods were employed to check the viability of the simulated skyrmions as a possible solution for the measured demagnetization fields from the g-CoPt films. In agreement with micromagnetic simulations, in reconstructed patterns, we observe small deviations of helicity from pure Bloch-type skyrmions characterized by the Bloch gauge, i.e., $\nabla \times \boldsymbol{m}_{x,y} = 0$; however, due to relatively large d_{NV} we are not able to make quantitative prediction of helicity from the reconstruction procedure. The inverse problem for finding $\boldsymbol{m}$ from the magnetic field maps can be written as[52]

$$B_\parallel(\boldsymbol{k}, d) = B_z(\boldsymbol{k}, d)(\cos(\theta_{NV}) - i\sin(\theta_{NV})\cos(\phi_k)) \quad (4)$$

$$B_z(\boldsymbol{k}, d) = \frac{\mu_0 M_s}{2}(e^{-dk} - e^{-(d+t)k})(-i\cos(\phi_k)m_x(\boldsymbol{k}) - i\sin(\phi_k)m_y(\boldsymbol{k}) + m_z(\boldsymbol{k})) \quad (5)$$

where the above equations define the kernels α_x, α_y, and α_z corresponding to convolutions in the x, y plane with m_x, m_y, and m_z, respectively, and $\boldsymbol{k}$ = ($k\cos(\phi_k)$, $k\sin(\phi_k)$) is the 2D vector in the reciprocal space.

A solution for the magnetization vector $\boldsymbol{m}$ determined up to the null space of the convolution (for example $\boldsymbol{m}_{x,y}$ of Bloch skyrmion solution corresponds to this null space)[52] is obtained through the implementation of a minimized cost function, achieving deconvolution with respect to the kernel. Combining this reconstruction with the normalization of vector $\boldsymbol{m}$ and boundary conditions, the magnetization m_z could be reconstructed and the helicity of skyrmions in g-CoPt single-layer film can be determined (see Methods). Figure 6 shows

https://doi.org/10.1021/acsnano.4c10145
ACS Nano 2024, 18, 31261−31273

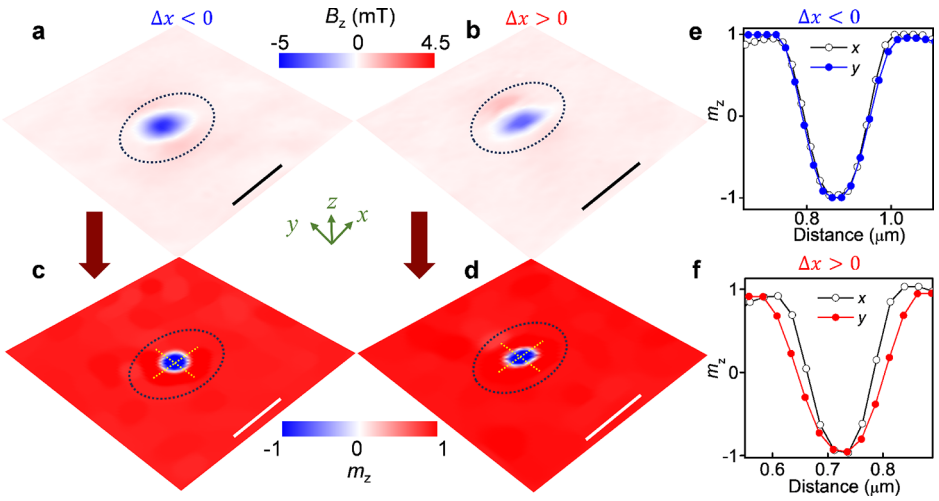

Figure 6. Magnetization reconstruction in the Bloch gauge. (a,b) B_z maps measured at H_{app} of 0.1 kOe and at a distance d_{NV} = 230 nm (200 nm) above isolated skyrmions on Δx = −50% (Δx = +50%) g-CoPt film. Subsequent analytical magnetization reconstruction images are shown in panels (c) and (d) corresponding to B_z images in panels (a) and (b), respectively. The scale bar in panels (a−d) is 500 nm. (e, f) Extracted magnetization profiles along x (open circle-scattered line) and y (filled circle- scattered line) directions from the reconstructed m_z images in panels (c) and (d).

the results of the reconstructed magnetization component obtained from the projected demagnetization field for g-CoPt films with Δx = −50% and Δx = +50%. Figure 6a,b show the NV stray field B_z component deduced from the isolated skyrmions in the g-CoPt (Δx = −50%) and g-CoPt (Δx = +50%) films shown in Figure 4d,f, respectively. The B_z component was obtained from NV measured $B_{||}$ image via a direct transformation made possible due to its linear dependence with the in-plane (B_x, B_y) components in Fourier space.[40] The corresponding magnetization m_z reconstruction 2D images are plotted in Figure 6c,d. Line profiles of the magnetization configurations are shown in Figure 6e,f, with cross sections being taken through the skyrmion core center in both the x and y directions on the g-CoPt (Δx = −50%) and g-CoPt (Δx = +50%) films, respectively.

The resulting normalized magnetization profile for m_z is an indication of the feasibility of the only solution with small deviations from the Bloch helicity; however, this also required slight adjustments of d_{NV} during the reconstruction as there is uncertainty in the experimental determination of this parameter. The reconstruction of the isolated skyrmion in Figure 6d exhibits rotational variance, which may be attributed to pinning sites, and is typical for skyrmions in the low field transitional regime between skyrmion and spiral phase. From the deconvolution procedure, it was also possible to reconstruct components m_x and m_y, through the normalization condition $|\boldsymbol{m}| = m_x^2 + m_y^2 + m_z^2 = 1$. Furthermore, it is reasonable to assume that the handedness of the stabilized skyrmions depends on the gradient polarity. However, due to the lack of dependence on the m_x and m_y terms in eq 5 for the Bloch skyrmion, handedness cannot be determined from the measured stray field maps.

In addition to the observation of near Bloch skyrmions in the g-CoPt single-layer films, the appearance of skyrmion pairs is reproducibly observed in MFM images for the g-CoPt (Δx = −50%) film across a wide range of magnetic fields (up to ±1.1 kOe), marked by stars in Figure 7a,b. There is also the presence of more complicated spin textures (seen in Figures 3a and 7a,b) whose morphology and topology may be determined by defects or disorder (see SI Section S8 and Figure S8.1). Similar behavior was observed in Ir/Fe/Co/Pt multilayers, in which wormlike magnetic features were ascribed to be merged Néel skyrmions with a topological charge equal to the number of skyrmions.[34] In comparison, the lower density of skyrmions in g-CoPt films would be less likely to form higher-order skyrmion chains.[34] To obtain additional information, a zoomed image of a skyrmion pair (marked by a green star in Figure 7a,b) is shown in Figure 7c, with cross sections along the center-to-center direction, plotted for a sequence of applied fields (Figure 7d). As the amplitude of H_{app} is increased, the individual radii of the pair skyrmions decrease, though the center-to-center distance remains constant, which may be a result of pinning behavior, which fixes the domain locally to a structural defect. Importantly, most pairs collapse above a certain applied magnetic field; see the pair highlighted by red and black stars in Figure 7a,b. This threshold annihilation behavior with H_{app} may be indicative of a competitive effect between dipolar interactions and magnetic anisotropy to stabilize different features such as skyrmion−antiskyrmion pairs.[16,60,62] Note that we use the term "skyrmion" to describe the observed (NV and MFM) isolated spin textures in g-CoPt single layers based on the presence of topological charge. A small number of spin textures may also have zero topological charge, and it might be warranted to refer to such textures as magnetic bubbles; see SI Section S8 and Figure S8.1.

A similar occurrence of spontaneously formed pairs is observed by NV-SPM. A large area NV PL map at H_{app} = 0.1 kOe is shown in Figure 7e, in which there are pairs as indicated by a dashed square in addition to isolated spots associated with skyrmions (see SI Section S7). Figure 7f displays a spatially resolved PL image of the pairs with a skyrmion distance of 450 nm. Considering that a significant stray-field $B_{||} \approx$ 15 mT at d_{NV} < 150 nm produced by these skyrmion pairs will significantly reduce NV ODMR contrast (Figure S6.2) related to PL quenching shown in Figure 7f. To measure the amplitude of the stray field $B_{||}$ along the NV axis, fully quantitative ODMR imaging taken at d_{NV} of 250 nm is performed in Figure 7g, corresponding to the pair imaged in Figure 7f. The skyrmion distance in the pair (450 nm) is higher than the d_{NV} of 250 nm, and the individual

https://doi.org/10.1021/acsnano.4c10145
ACS Nano 2024, 18, 31261−31273

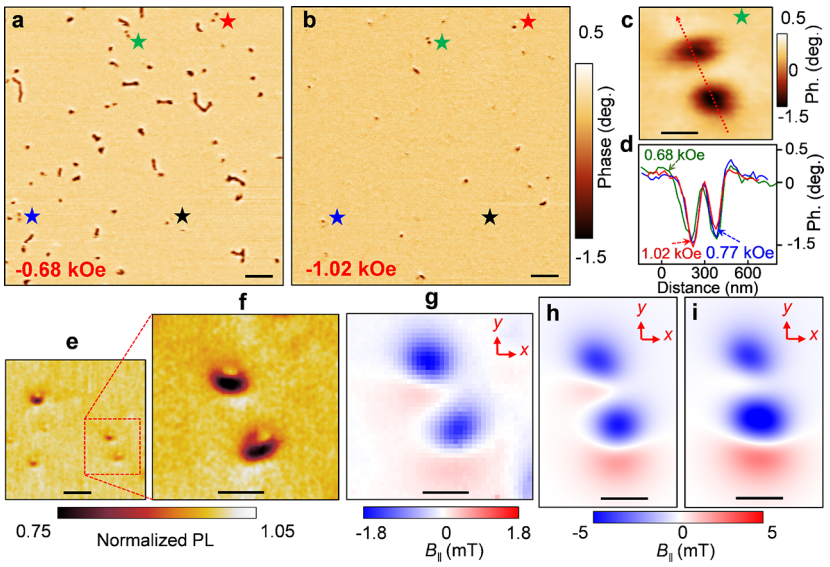

Figure 7. Observation of skyrmion pairs by MFM and NV-SPM in g-CoPt (Δx= −50%) single layer. (a,b) MFM images of skyrmion pairs (filled colored stars) at H_{app} of −0.68 and −1.02 kOe, respectively. The scale bar is 1 μm. (c) Zoomed image of the individual skyrmion pair indicated with a green star in panels (a) and (b). The scale bar is 100 nm. (d) Line cuts through the pair (red dashed arrow in panel (c)) for H_{app} of −0.68, −0.77, and −1.02 kOe. (e) NV PL quenching image of skyrmions at a standoff d_{NV} of 100 nm and H_{app} of 0.1 kOe. The scale bar is 1 μm. (f) Zoomed image of skyrmion pair indicated by dashed square in panel (e), taken at d_{NV} of 100 nm below the distance between the pair (~450 nm). The scale bar is 500 nm. (g) $B_{\parallel}$ map of the pair in panel (f), taken at a d_{NV} of 250 nm. The scale bar is 500 nm. Simulated magnetic stray field maps for pinned skyrmion−antiskyrmion (h) and skyrmion−skyrmion (i) pairs at a measurement height of 300 nm. The scale bars in panels (h) and (i) are 500 nm.

demagnetization fields can be resolved. As shown in Figure 7g, the $B_{\parallel}$ amplitude produced by the individual components of the pairs is similar to a slight change of the magnetic pattern, which may be related to the presence of different topological solitons such as skyrmions and antiskyrmions stabilized mainly by dipolar interactions in the g-CoPt single layer.[62] It is known that skyrmions and antiskyrmions can be stabilized by anisotropic DMI or dipolar interactions.[16,60,63] Based on micromagnetic simulations, skyrmion−antiskyrmion pairs as well as skyrmion−skyrmion pairs can be stabilized when pinned by disorder. Figure 7h shows the calculated $B_{\parallel}$ images for the simulated skyrmion−antiskyrmion pair and it qualitatively agrees with the NV-measured $B_{\parallel}$ map in Figure 7g. Pinned skyrmion−skyrmion pairs can also be stabilized in simulations, as shown in Figure 7i, with a slight change in the radius and magnetic stray-field pattern of each skyrmion. The underlying simulated magnetization (Figure S8.3), as well as calculated $B_{\parallel}$ maps of these systems at lower standoffs d_{NV} (Figure S8.4), are shown in the SI, Section S8. The stability of higher-order topological spin textures (winding number of 2) is also discussed and shown in Figure S8.4. The results of the simulations imply that the inclusion of disorder can influence the resulting magnetic texture in a way that allows for a more diverse set of topological magnetic structures to stabilize. Such spin texture systems may exhibit dynamic properties that are influenced by the local pinning energy landscape, including modification of the skyrmion Hall angle or distortion of the skyrmion morphology upon application of current.[64]

CONCLUSIONS

To summarize, we investigated the spin texture of the topologically protected skyrmions in g-CoPt single layers with gradient DMI by using NV scanning magnetometry. Skyrmions remain stable over a wide range of applied magnetic fields and are confirmed to be nearly Bloch-type from micromagnetic simulation and analytical magnetization reconstruction profiles extracted from NV magnetic images. The stabilization of pairs is also observed which may be explained by the formation of skyrmion−antiskyrmion[62] or skyrmion−skyrmion[65] pairs, or higher-order skyrmions[34] stabilized by dipolar magnetic interaction and pinned by disorder. Our findings highlight engineered DMI through the gradient composition as an alternative tool to control skyrmions in magnetic materials in a continuous manner.[66] Due to the proportionality between the effective gradient parameter $\Delta x/t$ and its resulting DMI strength, it is possible to further increase the DMI (i.e., through reduction of the thickness for a given gradient amount) and study its effect on skyrmions.[25] Potentially, in combination with sufficiently low disorder, it may be possible to observe the DMI threshold above which the skyrmions form a lattice. Furthermore, the ability to tune the PMA and SOC strength by means of gradient sign and choice of elements makes gradient DMI in conjunction with NV-SPM an excellent platform for fundamental skyrmionics research.

Other interesting effects arising from the nontrivial topology of skyrmions are their dynamics in the presence of spin-polarized current such as the skyrmion Hall effect.[67] Future magneto-transport experiments combined with NV-SPM[68] by measuring the motion and velocity of skyrmion pairs observed in the g-CoPt films can elucidate the type of these spin textures and their respective velocities as a function of the applied magnetic field and film thickness, which may be relevant for application in race-track memories.[2]

METHODS

Sample Preparation. Stacks with SiO_2 (2 nm)/ Co_xPt_{1-x} (10 nm) and a calibration sample Pt (2 nm)/MgO (2 nm)/Co_3Pt (4 nm) were deposited by d.c. and radio frequency magnetron sputtering (Kurt J. Lesker) on a $SrTiO_3$ (STO) (111) single-crystal substrate.

https://doi.org/10.1021/acsnano.4c10145
ACS Nano 2024, 18, 31261−31273

During the growth of Co_xPt_{1-x} with a composition gradient (g-CoPt), the relative deposition rates of the Co and Pt elements are linearly changed, resulting in a linear composition-magnetization difference along the growth direction. During the growth of the calibration sample Co_3Pt, the fixed deposition rates of the Co and Pt elements were employed. The base pressures were lower than 4×10^{-8} Torr. During the deposition process of g-CoPt single layers, the temperature was kept at 280 °C and the Ar gas pressure was kept constant at 6×10^{-3} Torr. The films were then cooled to room temperature, and a 2 nm SiO_2 (MgO) capping layer was deposited by radio frequency magnetron sputtering to prevent any oxidation effect.

X-ray Diffraction. X-ray diffraction measurements (θ–2θ scan) were performed on positive ($\Delta x = +50\%$) and negative ($\Delta x = -50\%$) composition gradient g-CoPt single layers (thickness of 10 nm) at room temperature at the Singapore Synchrotron light source with an X-ray wavelength of 1.541 Å.

Device Fabrication and Transport Measurement. The SiO_2 (2 nm)/ Co_xPt_{1-x} (10 nm) films with composition gradient Δx = +50% (− 50%) were patterned into a Hall bar device with a width of 5 μm and length of 40 μm by using an Ultraviolet Maskless Lithography machine (TuoTuo Technology) and ion beam etching technology. A calibration sample Pt (2 nm)/MgO (2 nm)/Co_3Pt (4 nm)/STO substrate was patterned into a stripe device with a width of 1 or 2 μm by electron-beam lithography (EBL) and ion beam etching technology. The measurement of Hall loops was conducted in a physical property measurement system (PPMS), in which a dc current of 100 μA was applied and Hall resistance ρ_{xy} can be read with a sweeping out-of-plane magnetic field. The magnetic hysteresis loops of unpatterned g-CoPt single-layer films with out-of-plane and in-plane magnetic fields were measured by SQUID (Quantum design MPMS3).

Brillouin Light Scattering. The BLS experiment is under the geometry of Damon-Eshbach (DE) spin-wave modes in all measurements, in which the magnetic field $\mu_0 H$ is applied along the film plane and DE spin-wave propagates perpendicularly to the $\mu_0 H$ direction. An s-polarized monochromatic laser beam with wavelength λ = 532 nm is focused onto the sample surface with an incident angle θ. The p-polarized backscattered light was collected and sent to a Sandercock-type multipass tandem Fabry–Perot interferometer. Owing to the conservation of momentum on the film plane, the Stokes (anti-Stokes) peak in the BLS spectra corresponds to the creation (annihilation) of magnons with momentum $k_x = \frac{4\pi}{\lambda}\sin\theta$. Due to the presence of the DMI, the counterpropagating DE spin waves became nonreciprocal, leading to the frequency shift (Δf). Then, the amplitude and sign of DMI could be quantified through a linear fitting of Δf vs k_x measured at negative and positive $\mu_0 H$.

Magnetic Force Microscopy. Magnetic force microscopy (MFM) images were obtained using a Digital Instruments IIIA atomic force microscope. The magnetic tips used were standard Si AFM tips coated with about 20 nm FePt layer and subsequently annealed at 650 °C to achieve a large coercivity of the deposited tip coating, giving a relatively low magnetic moment of $\sim 10^{-14}$ emu at the end of the tip. The cantilever was magnetized along the out-of-plane direction under a 3 T magnetic field, ensuring that uniaxial magnetization preserves the relative phase contrast during the measurement under the magnetic field. MFM images were taken in double-pass mode with a lift height of 30 nm.

Optically Detected Magnetic Resonance Imaging. NV stray magnetic field images were obtained using a home-built nitrogen vacancy-scanning probe microscope (NV-SPM) with combined confocal and atomic force microscope functionality.[49,57] Single NV probes were purchased from Qnami with a ^{15}N implantation energy of 12 keV, corresponding to an implantation distance of around 12 nm from the apex of the diamond tip. The negatively charged NV center, composed of a substitutional nitrogen atom adjacent to a vacancy site, is an electronic spin 1 with a spin-triplet ($|m_S = 0\rangle$, $|m_S = \pm 1\rangle$) in the ground state. 532 nm laser illumination induces spin-dependent photoluminescence (650–800 nm) allowing optical detected magnetic resonance (ODMR) of its spin state. The applied magnetic field H_{app}, provided by a permanent magnet, splits $|m_S = \pm 1\rangle$ state via the Zeeman effect and leads to two ($|m_S = 0\rangle$ to $|m_S = -1\rangle$ and $|m_S = 0\rangle$ to $|m_S = +1\rangle$) ODMR peaks whose frequencies depend on the projection of the field along the NV symmetry axis. During ODMR imaging, the $|m_S = 0\rangle$ to $|m_S = +1\rangle$ spin resonance spectrum is obtained at each pixel of the sample area and the Zeeman splitting is measured, creating an image of the resulting Lorentzian center frequency shift. The setup is integrated with microwave (MW) equipment to monitor NV spin transitions and with a single photon counter module (SPCM) coupled with a single-mode fiber.[37,49,56] The objective used was a 6 mm WD, 0.7 NA Mitutoyo objective, which allowed for flexibility of setup considering the tip and MW antenna placement. ANP-101 nanopositioners from attocube were used for course positioning of the tip during the approach. The sample is rastered by a closed loop three-axis piezo stage (NPXY100Z10–128), with the diamond tip fixed.

Micromagnetic Simulations. To model the magnetic skyrmions measured by NV-SPM, we performed micromagnetic simulations using the GPU-based platform Mumax3.[69] The simulations were carried out using the magnetic parameters (M_s, K_u) of the negative Δx = −50% and positive Δx = +50% g-CoPt films (thickness of 10 nm), obtained from SQUID measurements. The position-dependent DMI was included phenomenologically using a function,[24] $C + D_b e^{-(z-z_b)/l} + D_t e^{-(z-z_t)/l}$, where D_b and D_t are the DMI amplitudes at the bottom and top interfaces of the CoPt film with coordinates z_b and z_t, respectively, which decay into the film interior (bulk) with a decay length l. The DMI contribution from the gradient-induced BMA, C *is* kept constant through the film thickness.[24] Periodic boundary conditions were imposed when simulating single skyrmions to prevent demagnetization effects at the edge. Key parameters to fit the NV and micromagnetic simulations are the NV standoff d_{NV}, NV polar (θ_{NV}), and azimuthal (ϕ_{NV}) angles relative to the Cartesian reference frame (x, y, z), Figure 4a. To measure these parameters, we used a calibration FM substrate composed of 1 μm wide Pt (2 nm)/MgO (2 nm)/Co_3Pt (4 nm)/STO stripes with high PMA. The fabrication details and magnetic properties of this sample are provided in the SI, Section S4.

Magnetization Reconstruction of Skyrmion Profiles from NV ODMR Images. We consider magnetic stray fields produced by magnetic dipoles confined within a magnetic film of thickness t. We disregard variations in M_s in the film since it has a small effect for $t \ll d_{NV}$. The stray fields are related to magnetization direction by the relation $\boldsymbol{B}(\boldsymbol{k}, d) = \hat{D}(\boldsymbol{k}, d)\ \boldsymbol{m}(\boldsymbol{k})$, where $\boldsymbol{m}(\boldsymbol{k})$ is the 2D Fourier transform of magnetization direction vector and $\boldsymbol{B}(\boldsymbol{k}, d)$ is the 2D Fourier transform of the magnetic field in the plane that is distance d away from the film. The kernel matrix $\hat{D}(\boldsymbol{k}, d)$ reads as

$$\hat{D}(\boldsymbol{k}, d) = \frac{\mu_0 M_s}{2}(e^{-dk} - e^{-(d+t)k}) \begin{pmatrix} -\cos^2(\phi_k) & -\frac{\sin(2\phi_k)}{2} & -i\cos(\phi_k) \\ -\frac{\sin(2\phi_k)}{2} & -\sin^2(\phi_k) & -i\sin(\phi_k) \\ -i\cos(\phi_k) & -i\sin(\phi_k) & 1 \end{pmatrix} \quad \text{(M1)}$$

where the rows of matrix $\hat{D}(\boldsymbol{k}, d)$ are linearly dependent. We rewrite eq M1 in real space as

$$B_{\parallel}(\rho) = \frac{\mu_0 M_s}{2}(\alpha_x {}^{*} m_x(\rho) + \alpha_y {}^{*} m_y(\rho) + \alpha_z {}^{*} m_z(\rho)) \quad \text{(M2)}$$

where the symbol * denotes the convolution, $\boldsymbol{\rho}$ defines a two-dimensional position within the reconstruction plane, and we define three convolution kernels α_x, α_y, and α_z. The analytical expressions for kernels can be easily calculated but are complicated, and we do not present them here. The solution of eq M2 for $\boldsymbol{m}(\boldsymbol{\rho})$ is not unique due to the nonvanishing null space of the kernels. The procedure was similar to ref 52. Nevertheless, ref 52 argued that enforcing normalization and skyrmion boundary conditions at $\rho \to \infty$ selects

https://doi.org/10.1021/acsnano.4c10145
ACS Nano 2024, 18, 31261–31273

one solution within the Bloch or Néel gauge. Here, a different cost minimization technique is utilized, which relied on the built-in function ImageDeconvolve in Wolfram Mathematica (https://www.wolfram.com/). Furthermore, ref 52 considered solutions deviating from the above gauges. In our heuristic approach, we directly minimize the following functional:

$$\mathcal{L} = \int \left(B_{\parallel}(\rho) - \frac{\mu_0 M_s}{2} \vec{\alpha} \times \boldsymbol{m}(\rho) \right)^2 \mathrm{d}\rho \tag{M3}$$

by using the built-in function ImageDeconvolve in Wolfram Mathematica. We observe that with enforced skyrmion boundary conditions, the minimization procedure chooses solutions that are very close to the Bloch-type solutions, which also agrees with our micromagnetic analysis (see the discussion above and in the SI, Section S8).

ASSOCIATED CONTENT

Supporting Information

The Supporting Information is available free of charge at https://pubs.acs.org/doi/10.1021/acsnano.4c10145.

Characterization (AFM, XRD) of g-CoPt single layer films; magnetic (THE, SQUID, MFM) characterization of g-CoPt (Δx = +50%) film; quantitative NV ODMR imaging; calibration of NV measurements: measuring the standoff and NV axis angles; vector reconstruction of skyrmion stray field components; height dependence in PL quenching imaging; corroboration of MFM and NV quenching imaging; and micromagnetic simulations (PDF)

AUTHOR INFORMATION

Corresponding Authors

Jingsheng Chen − *Department of Materials Science and Engineering, National University of Singapore, Singapore 117579, Singapore; National University of Singapore (Suzhou) Research Institute, Suzhou, Jiangsu 215123, China;* orcid.org/0000-0003-3188-2803; Email: msecj@nus.edu.sg

Abdelghani Laraoui − *Department of Mechanical & Materials Engineering, University of Nebraska-Lincoln, Lincoln, Nebraska 68588, United States; Department of Physics and Astronomy and the Nebraska Center for Materials and Nanoscience, University of Nebraska-Lincoln, Lincoln, Nebraska 68588, United States;* orcid.org/0000-0002-2811-8030; Email: alaraoui2@unl.edu

Authors

Adam Erickson − *Department of Mechanical & Materials Engineering, University of Nebraska-Lincoln, Lincoln, Nebraska 68588, United States*

Qihan Zhang − *Department of Materials Science and Engineering, National University of Singapore, Singapore 117579, Singapore*

Hamed Vakili − *Department of Physics and Astronomy and the Nebraska Center for Materials and Nanoscience, University of Nebraska-Lincoln, Lincoln, Nebraska 68588, United States*

Chaozhong Li − *Key Laboratory for Magnetism and Magnetic Materials of Ministry of Education, School of Physical Science and Technology, Lanzhou University, Lanzhou 730000, China*

Suchit Sarin − *Department of Mechanical & Materials Engineering, University of Nebraska-Lincoln, Lincoln, Nebraska 68588, United States*

Suvechhya Lamichhane − *Department of Physics and Astronomy and the Nebraska Center for Materials and Nanoscience, University of Nebraska-Lincoln, Lincoln, Nebraska 68588, United States*

Lanxin Jia − *Department of Materials Science and Engineering, National University of Singapore, Singapore 117579, Singapore;* orcid.org/0009-0004-9329-6396

Ilja Fescenko − *Laser Center, University of Latvia, Riga LV-1004, Latvia*

Edward Schwartz − *Department of Physics and Astronomy and the Nebraska Center for Materials and Nanoscience, University of Nebraska-Lincoln, Lincoln, Nebraska 68588, United States*

Sy-Hwang Liou − *Department of Physics and Astronomy and the Nebraska Center for Materials and Nanoscience, University of Nebraska-Lincoln, Lincoln, Nebraska 68588, United States*

Jeffrey E. Shield − *Department of Mechanical & Materials Engineering, University of Nebraska-Lincoln, Lincoln, Nebraska 68588, United States*

Guozhi Chai − *Key Laboratory for Magnetism and Magnetic Materials of Ministry of Education, School of Physical Science and Technology, Lanzhou University, Lanzhou 730000, China*

Alexey A. Kovalev − *Department of Physics and Astronomy and the Nebraska Center for Materials and Nanoscience, University of Nebraska-Lincoln, Lincoln, Nebraska 68588, United States*

Complete contact information is available at: https://pubs.acs.org/10.1021/acsnano.4c10145

Author Contributions

†A.E., Q.Z., and H.V. contributed equally.

Author Contributions

A.E. performed NV-SPM and MFM measurements and analyzed the data; Q.Z, grew the g-CoPt films and performed topography (AFM), XRD, MOKE, SQUID, AHE, and THE measurements; H.V., E.S., and A.A.K. performed micromagnetic modeling and magnetization reconstruction analysis; C.L. and G.C. performed BLS measurements; S.S. and J.E.S. performed HAADF-STEM and EDS on the graded CoPt films; S.L. and S.-Y.L. assisted A.E in MFM measurements; L.J. helped to prepare the CoPt stripe device by EBL; I.F. created code for recovering vector stray-field components and analyzed NV-ODMR images. J.C. and A.L. designed the experiments and supervised the project. A.E. and A.L. wrote the paper with contributions and feedback from all authors.

Notes

The authors declare no competing financial interest.

ACKNOWLEDGMENTS

A.L., A.A.K., and S.-H.L. acknowledge support by the National Science Foundation EPSCoR RII Track-1: Emergent Quantum Materials and Technologies (EQUATE), Award OIA-2044049. The research done at the University of Nebraska-Lincoln was performed in part in the Nebraska Nanoscale Facility: National Nanotechnology Coordinated Infrastructure and the Nebraska Center for Materials and Nanoscience (and/or NERCF), supported by the National Science Foundation

ECCS under Award 2025298. The research performed at the National University of Singapore was supported by the Singapore Ministry of Education under awards: MOE-T2EP50223-0006, MOE-T2EP50123-0012, MOE-T2EP50121-0011, and MOE Tier 1:22-4888-A0001. I.F. acknowledges support from the Latvian Quantum Initiative under European Union Recovery and Resilience Facility project no. 2.3.1.1.i.0/1/22/I/CFLA/001.

REFERENCES

(1) Fert, A.; Reyren, N.; Cros, V. Magnetic Skyrmions: Advances in Physics and Potential Applications. *Nat. Rev. Mater.* **2017**, *2*, 17031.
(2) Fert, A.; Cros, V.; Sampaio, J. *Skyrmions on the Track. Nature Nanotech* **2013**, *8*, 152−156.
(3) Li, S.; Kang, W.; Huang, Y.; Zhang, X.; Zhou, Y.; Zhao, W. Magnetic Skyrmion-Based Artificial Neuron Device. *Nanotechnology* **2017**, *28*, 31LT01.
(4) Huang, Y.; Kang, W.; Zhang, X.; Zhou, Y.; Zhao, W. Magnetic Skyrmion-Based Synaptic Devices. *Nanotechnology* **2017**, *28*, No. 08LT02.
(5) Moriya, T. Anisotropic Superexchange Interaction and Weak Ferromagnetism. *Phys. Rev.* **1960**, *120* (1), 91−98.
(6) Dzyaloshinsky, I. A Thermodynamic Theory of "Weak" Ferromagnetism of Antiferromagnetics. *J. Phys. Chem. Solids* **1958**, *4*, 241−255.
(7) Soumyanarayanan, A.; Raju, M.; Gonzalez Oyarce, A. L.; Tan, A. K. C.; Im, M.-Y.; Petrović, A. P.; Ho, P.; Khoo, K. H.; Tran, M.; Gan, C. K.; Ernult, F.; Panagopoulos, C. Tunable Room-Temperature Magnetic Skyrmions in Ir/Fe/Co/Pt Multilayers. *Nat. Mater.* **2017**, *16*, 898−904.
(8) Heinze, S.; Von Bergmann, K.; Menzel, M.; Brede, J.; Kubetzka, A.; Wiesendanger, R.; Bihlmayer, G.; Blügel, S. Spontaneous Atomic-Scale Magnetic Skyrmion Lattice in Two Dimensions. *Nature Phys.* **2011**, *7*, 713−718.
(9) Romming, N.; Hanneken, C.; Menzel, M.; Bickel, J. E.; Wolter, B.; Von Bergmann, K.; Kubetzka, A.; Wiesendanger, R. Writing and Deleting Single Magnetic Skyrmions. *Science* **2013**, *341* (6146), 636−639.
(10) Moreau-Luchaire, C.; Moutafis, C.; Reyren, N.; Sampaio, J.; Vaz, C. A. F.; Van Horne, N.; Bouzehouane, K.; Garcia, K.; Deranlot, C.; Warnicke, P.; Wohlhüter, P.; George, J.-M.; Weigand, M.; Raabe, J.; Cros, V.; Fert, A. Additive Interfacial Chiral Interaction in Multilayers for Stabilization of Small Individual Skyrmions at Room Temperature. *Nat. Nanotechnol.* **2016**, *11*, 444−448.
(11) Woo, S.; Litzius, K.; Krüger, B.; Im, M.-Y.; Caretta, L.; Richter, K.; Mann, M.; Krone, A.; Reeve, R. M.; Weigand, M.; Agrawal, P.; Lemesh, I.; Mawass, M.-A.; Fischer, P.; Kläui, M.; Beach, G. S. D. Observation of Room-Temperature Magnetic Skyrmions and Their Current-Driven Dynamics in Ultrathin Metallic Ferromagnets. *Nat. Mater.* **2016**, *15*, 501−506.
(12) Boulle, O.; Vogel, J.; Yang, H.; Pizzini, S.; De Souza Chaves, D.; Locatelli, A.; Menteş, T. O.; Sala, A.; Buda-Prejbeanu, L. D.; Klein, O.; Belmeguenai, M.; Roussigné, Y.; Stashkevich, A.; Chérif, S. M.; Aballe, L.; Foerster, M.; Chshiev, M.; Auffret, S.; Miron, I. M.; Gaudin, G. Room-Temperature Chiral Magnetic Skyrmions in Ultrathin Magnetic Nanostructures. *Nat. Nanotechnol.* **2016**, *11*, 449−454.
(13) Li, Y.; Kanazawa, N.; Yu, X. Z.; Tsukazaki, A.; Kawasaki, M.; Ichikawa, M.; Jin, X. F.; Kagawa, F.; Tokura, Y. Robust Formation of Skyrmions and Topological Hall Effect Anomaly in Epitaxial Thin Films of MnSi. *Phys. Rev. Lett.* **2013**, *110* (11), No. 117202.
(14) Yu, X. Z.; Onose, Y.; Kanazawa, N.; Park, J. H.; Han, J. H.; Matsui, Y.; Nagaosa, N.; Tokura, Y. Real-Space Observation of a Two-Dimensional Skyrmion Crystal. *Nature* **2010**, *465*, 901−904.
(15) Yu, X. Z.; Kanazawa, N.; Onose, Y.; Kimoto, K.; Zhang, W. Z.; Ishiwata, S.; Matsui, Y.; Tokura, Y. Near Room-Temperature Formation of a Skyrmion Crystal in Thin-Films of the Helimagnet FeGe. *Nat. Mater.* **2011**, *10*, 106−109.
(16) Zheng, F.; Kiselev, N. S.; Yang, L.; Kuchkin, V. M.; Rybakov, F. N.; Blügel, S.; Dunin-Borkowski, R. E. Skyrmion−Antiskyrmion Pair Creation and Annihilation in a Cubic Chiral Magnet. *Nat. Phys.* **2022**, *18*, 863−868.
(17) Wang, W.; Song, D.; Wei, W.; Nan, P.; Zhang, S.; Ge, B.; Tian, M.; Zang, J.; Du, H. Electrical Manipulation of Skyrmions in a Chiral Magnet. *Nat. Commun.* **2022**, *13*, 1593.
(18) Zhang, Y.; Tang, J.; Wu, Y.; Shi, M.; Xu, X.; Wang, S.; Tian, M.; Du, H. Stable Skyrmion Bundles at Room Temperature and Zero Magnetic Field in a Chiral Magnet. *Nat. Commun.* **2024**, *15*, 3391.
(19) Bogdanov, A. N.; Rößler, U. K.; Wolf, M.; Müller, K.-H. Magnetic Structures and Reorientation Transitions in Noncentrosymmetric Uniaxial Antiferromagnets. *Phys. Rev. B* **2002**, *66* (21), No. 214410.
(20) Vir, P.; Kumar, N.; Borrmann, H.; Jamijansuren, B.; Kreiner, G.; Shekhar, C.; Felser, C. Tetragonal Superstructure of the Antiskyrmion Hosting Heusler Compound $Mn_{1.4}PtSn$. *Chem. Mater.* **2019**, *31* (15), 5876−5880.
(21) Ma, T.; Sharma, A. K.; Saha, R.; Srivastava, A. K.; Werner, P.; Vir, P.; Kumar, V.; Felser, C.; Parkin, S. S. P. Tunable Magnetic Antiskyrmion Size and Helical Period from Nanometers to Micrometers in a D_{2d} Heusler Compound. *Adv. Mater.* **2020**, *32* (28), 2002043.
(22) Peng, L.; Takagi, R.; Koshibae, W.; Shibata, K.; Nakajima, K.; Arima, T.; Nagaosa, N.; Seki, S.; Yu, X.; Tokura, Y. Controlled Transformation of Skyrmions and Antiskyrmions in a Non-Centrosymmetric Magnet. *Nat. Nanotechnol.* **2020**, *15*, 181−186.
(23) Nayak, A. K.; Kumar, V.; Ma, T.; Werner, P.; Pippel, E.; Sahoo, R.; Damay, F.; Rößler, U. K.; Felser, C.; Parkin, S. S. P. Magnetic Antiskyrmions above Room Temperature in Tetragonal Heusler Materials. *Nature* **2017**, *548*, 561−566.
(24) Liang, J.; Chshiev, M.; Fert, A.; Yang, H. Gradient-Induced Dzyaloshinskii−Moriya Interaction. *Nano Lett.* **2022**, *22* (24), 10128−10133.
(25) Zhang, Q.; Liang, J.; Bi, K.; Zhao, L.; Bai, H.; Cui, Q.; Zhou, H.-A.; Bai, H.; Feng, H.; Song, W.; Chai, G.; Gladii, O.; Schultheiss, H.; Zhu, T.; Zhang, J.; Peng, Y.; Yang, H.; Jiang, W. Quantifying the Dzyaloshinskii-Moriya Interaction Induced by the Bulk Magnetic Asymmetry. *Phys. Rev. Lett.* **2022**, *128* (16), No. 167202.
(26) Zheng, Z.; Zhang, Y.; Lopez-Dominguez, V.; Sánchez-Tejerina, L.; Shi, J.; Feng, X.; Chen, L.; Wang, Z.; Zhang, Z.; Zhang, K.; Hong, B.; Xu, Y.; Zhang, Y.; Carpentieri, M.; Fert, A.; Finocchio, G.; Zhao, W.; Khalili Amiri, P. Field-Free Spin-Orbit Torque-Induced Switching of Perpendicular Magnetization in a Ferrimagnetic Layer with a Vertical Composition Gradient. *Nat. Commun.* **2021**, *12*, 4555.
(27) Liu, L.; Zhou, C.; Zhao, T.; Yao, B.; Zhou, J.; Shu, X.; Chen, S.; Shi, S.; Xi, S.; Lan, D.; Lin, W.; Xie, Q.; Ren, L.; Luo, Z.; Sun, C.; Yang, P.; Guo, E.-J.; Dong, Z.; Manchon, A.; Chen, J. Current-Induced Self-Switching of Perpendicular Magnetization in CoPt Single Layer. *Nat. Commun.* **2022**, *13*, 3539.
(28) Fert, A.; Levy, P. M. Role of Anisotropic Exchange Interactions in Determining the Properties of Spin-Glasses. *Phys. Rev. Lett.* **1980**, *44* (23), 1538−1541.
(29) Rajput, N. S.; Sloyan, K.; Anjum, D. H.; Chiesa, M.; Ghaferi, A. A. A User-Friendly FIB Lift-out Technique to Prepare Plan-View TEM Sample of 2D Thin Film Materials. *Ultramicroscopy* **2022**, *235*, No. 113496.
(30) Cortés-Ortuño, D.; Landeros, P. Influence of the Dzyaloshinskii−Moriya Interaction on the Spin-Wave Spectra of Thin Films. *J. Phys.: Condens. Matter* **2013**, *25*, 156001.
(31) Belmeguenai, M.; Adam, J.-P.; Roussigné, Y.; Eimer, S.; Devolder, T.; Kim, J.-V.; Cherif, S. M.; Stashkevich, A.; Thiaville, A. Interfacial Dzyaloshinskii-Moriya Interaction in Perpendicularly Magnetized $Pt/Co/AlO_x$ Ultrathin Films Measured by Brillouin Light Spectroscopy. *Phys. Rev. B* **2015**, *91* (18), No. 180405.
(32) Di, K.; Zhang, V. L.; Lim, H. S.; Ng, S. C.; Kuok, M. H.; Qiu, X.; Yang, H. Asymmetric Spin-Wave Dispersion Due to Dzyaloshinskii-Moriya Interaction in an Ultrathin Pt/CoFeB Film. *Appl. Phys. Lett.* **2015**, *106* (5), No. 052403.

https://doi.org/10.1021/acsnano.4c10145
ACS Nano 2024, 18, 31261−31273

(33) Zheng, F.; Li, H.; Wang, S.; Song, D.; Jin, C.; Wei, W.; Kovács, A.; Zang, J.; Tian, M.; Zhang, Y.; Du, H.; Dunin-Borkowski, R. E. Direct Imaging of a Zero-Field Target Skyrmion and Its Polarity Switch in a Chiral Magnetic Nanodisk. *Phys. Rev. Lett.* **2017**, *119* (19), No. 197205.
(34) Raju, M.; Yagil, A.; Soumyanarayanan, A.; Tan, A. K. C.; Almoalem, A.; Ma, F.; Auslaender, O. M.; Panagopoulos, C. The Evolution of Skyrmions in Ir/Fe/Co/Pt Multilayers and Their Topological Hall Signature. *Nat. Commun.* **2019**, *10*, 696.
(35) Liou, S.-H. Advanced Magnetic Force Microscopy Tips for Imaging Domains. In *Handbook of Advanced Magnetic Materials*; Liu, Y.; Sellmyer, D. J.; Shindo, D., Eds.; Springer US: Boston, MA, 2006; pp 374−396.
(36) Casiraghi, A.; Corte-León, H.; Vafaee, M.; Garcia-Sanchez, F.; Durin, G.; Pasquale, M.; Jakob, G.; Kläui, M.; Kazakova, O. Individual Skyrmion Manipulation by Local Magnetic Field Gradients. *Commun. Phys.* **2019**, *2*, 145.
(37) Laraoui, A.; Hodges, J. S.; Meriles, C. A. Magnetometry of Random Ac Magnetic Fields Using a Single Nitrogen-Vacancy Center. *Appl. Phys. Lett.* **2010**, *97* (14), 143104.
(38) Maletinsky, P.; Hong, S.; Grinolds, M. S.; Hausmann, B.; Lukin, M. D.; Walsworth, R. L.; Loncar, M.; Yacoby, A. A Robust Scanning Diamond Sensor for Nanoscale Imaging with Single Nitrogen-Vacancy Centres. *Nat. Nanotechnol.* **2012**, *7*, 320−324.
(39) Rondin, L.; Tetienne, J.-P.; Hingant, T.; Roch, J.-F.; Maletinsky, P.; Jacques, V. Magnetometry with Nitrogen-Vacancy Defects in Diamond. *Rep. Prog. Phys.* **2014**, *77*, No. 056503.
(40) Casola, F.; Van Der Sar, T.; Yacoby, A. Probing Condensed Matter Physics with Magnetometry Based on Nitrogen-Vacancy Centres in Diamond. *Nat. Rev. Mater.* **2018**, *3*, 17088.
(41) Laraoui, A.; Ambal, K. Opportunities for Nitrogen-Vacancy-Assisted Magnetometry to Study Magnetism in 2D van Der Waals Magnets. *Appl. Phys. Lett.* **2022**, *121* (6), No. 060502.
(42) Timalsina, R.; Wang, H.; Giri, B.; Erickson, A.; Xu, X.; Laraoui, A. Mapping of Spin-Wave Transport in Thulium Iron Garnet Thin Films Using Diamond Quantum Microscopy. *Adv. Elect Materials* **2023**, *10* (3), 2300648.
(43) Lamichhane, S.; McElveen, K. A.; Erickson, A.; Fescenko, I.; Sun, S.; Timalsina, R.; Guo, Y.; Liou, S.-H.; Lai, R. Y.; Laraoui, A. Nitrogen-Vacancy Magnetometry of Individual Fe-Triazole Spin Crossover Nanorods. *ACS Nano* **2023**, *17* (9), 8694−8704.
(44) Doherty, M. W.; Manson, N. B.; Delaney, P.; Jelezko, F.; Wrachtrup, J.; Hollenberg, L. C. L. The Nitrogen-Vacancy Colour Centre in Diamond. *Phys. Rep.* **2013**, *528* (1), 1−45.
(45) Thiel, L.; Rohner, D.; Ganzhorn, M.; Appel, P.; Neu, E.; Müller, B.; Kleiner, R.; Koelle, D.; Maletinsky, P. Quantitative Nanoscale Vortex Imaging Using a Cryogenic Quantum Magnetometer. *Nat. Nanotechnol.* **2016**, *11*, 677−681.
(46) Appel, P.; Shields, B. J.; Kosub, T.; Hedrich, N.; Hübner, R.; Faßbender, J.; Makarov, D.; Maletinsky, P. Nanomagnetism of Magnetoelectric Granular Thin-Film Antiferromagnets. *Nano Lett.* **2019**, *19* (3), 1682−1687.
(47) Thiel, L.; Wang, Z.; Tschudin, M. A.; Rohner, D.; Gutiérrez-Lezama, I.; Ubrig, N.; Gibertini, M.; Giannini, E.; Morpurgo, A. F.; Maletinsky, P. Probing Magnetism in 2D Materials at the Nanoscale with Single-Spin Microscopy. *Science* **2019**, *364* (6444), 973−976.
(48) Finco, A.; Haykal, A.; Tanos, R.; Fabre, F.; Chouaieb, S.; Akhtar, W.; Robert-Philip, I.; Legrand, W.; Ajejas, F.; Bouzehouane, K.; Reyren, N.; Devolder, T.; Adam, J.-P.; Kim, J.-V.; Cros, V.; Jacques, V. Imaging Non-Collinear Antiferromagnetic Textures via Single Spin Relaxometry. *Nat. Commun.* **2021**, *12*, 767.
(49) Erickson, A.; Shah, S. Q. A.; Mahmood, A.; Fescenko, I.; Timalsina, R.; Binek, C.; Laraoui, A. Nanoscale Imaging of Antiferromagnetic Domains in Epitaxial Films of Cr_2O_3 via Scanning Diamond Magnetic Probe Microscopy. *RSC Adv.* **2022**, *13*, 178−185.
(50) Zhou, T. X.; Carmiggelt, J. J.; Gächter, L. M.; Esterlis, I.; Sels, D.; Stöhr, R. J.; Du, C.; Fernandez, D.; Rodriguez-Nieva, J. F.; Büttner, F.; Demler, E.; Yacoby, A. A Magnon Scattering Platform. *Proc. Natl. Acad. Sci. U. S. A.* **2021**, *118* (25), No. e2019473118.
(51) Simon, B. G.; Kurdi, S.; Carmiggelt, J. J.; Borst, M.; Katan, A. J.; van der Sar, T. Filtering and Imaging of Frequency-Degenerate Spin Waves Using Nanopositioning of a Single-Spin Sensor. *Nano Lett.* **2022**, *22* (22), 9198−9204.
(52) Dovzhenko, Y.; Casola, F.; Schlotter, S.; Zhou, T. X.; Büttner, F.; Walsworth, R. L.; Beach, G. S. D.; Yacoby, A. Magnetostatic Twists in Room-Temperature Skyrmions Explored by Nitrogen-Vacancy Center Spin Texture Reconstruction. *Nat. Commun.* **2018**, *9*, 2712.
(53) Rana, K. G.; Finco, A.; Fabre, F.; Chouaieb, S.; Haykal, A.; Buda-Prejbeanu, L. D.; Fruchart, O.; Le Denmat, S.; David, P.; Belmeguenai, M.; Denneulin, T.; Dunin-Borkowski, R. E.; Gaudin, G.; Jacques, V.; Boulle, O. Room-Temperature Skyrmions at Zero Field in Exchange-Biased Ultrathin Films. *Phys. Rev. Applied* **2020**, *13* (4), No. 044079.
(54) Gross, I.; Martínez, L. J.; Tetienne, J.-P.; Hingant, T.; Roch, J.-F.; Garcia, K.; Soucaille, R.; Adam, J. P.; Kim, J.-V.; Rohart, S.; Thiaville, A.; Torrejon, J.; Hayashi, M.; Jacques, V. Direct Measurement of Interfacial Dzyaloshinskii-Moriya Interaction in X |CoFeB| MgO Heterostructures with a Scanning NV Magnetometer (X = Ta, TaN, and W). *Phys. Rev. B* **2016**, *94* (6), No. 064413.
(55) Akhtar, W.; Hrabec, A.; Chouaieb, S.; Haykal, A.; Gross, I.; Belmeguenai, M.; Gabor, M. S.; Shields, B.; Maletinsky, P.; Thiaville, A.; Rohart, S.; Jacques, V. Current-Induced Nucleation and Dynamics of Skyrmions in a Co -Based Heusler Alloy. *Phys. Rev. Applied* **2019**, *11* (3), No. 034066.
(56) Laraoui, A.; Aycock-Rizzo, H.; Gao, Y.; Lu, X.; Riedo, E.; Meriles, C. A. Imaging Thermal Conductivity with Nanoscale Resolution Using a Scanning Spin Probe. *Nat. Commun.* **2015**, *6*, 8954.
(57) Erickson, A.; Shah, S. Q. A.; Mahmood, A.; Buragohain, P.; Fescenko, I.; Gruverman, A.; Binek, C.; Laraoui, A. Imaging Local Effects of Voltage and Boron Doping on Spin Reversal in Antiferromagnetic Magnetoelectric Cr_2O_3 Thin Films and Devices. *Adv. Funct Materials* **2024**, 2408542.
(58) Appel, P.; Neu, E.; Ganzhorn, M.; Barfuss, A.; Batzer, M.; Gratz, M.; Tschöpe, A.; Maletinsky, P. Fabrication of All Diamond Scanning Probes for Nanoscale Magnetometry. *Rev. Sci. Instrum.* **2016**, *87* (6), No. 063703.
(59) Tetienne, J.-P.; Rondin, L.; Spinicelli, P.; Chipaux, M.; Debuisschert, T.; Roch, J.-F.; Jacques, V. Magnetic-Field-Dependent Photodynamics of Single NV Defects in Diamond: An Application to Qualitative All-Optical Magnetic Imaging. *New J. Phys.* **2012**, *14*, 103033.
(60) Kovalev, A. A.; Sandhoefner, S. Skyrmions and Antiskyrmions in Quasi-Two-Dimensional Magnets. *Front. Phys.* **2018**, *6*, 98.
(61) Güngördü, U.; Nepal, R.; Tretiakov, O. A.; Belashchenko, K.; Kovalev, A. A. Stability of Skyrmion Lattices and Symmetries of Quasi-Two-Dimensional Chiral Magnets. *Phys. Rev. B* **2016**, *93* (6), No. 064428.
(62) Koshibae, W.; Nagaosa, N. Theory of Antiskyrmions in Magnets. *Nat. Commun.* **2016**, *7*, 10542.
(63) Goerzen, M. A.; Von Malottki, S.; Meyer, S.; Bessarab, P. F.; Heinze, S. Lifetime of Coexisting Sub-10 Nm Zero-Field Skyrmions and Antiskyrmions. *npj Quantum Mater.* **2023**, *8*, 54.
(64) Gruber, R.; Zázvorka, J.; Brems, M. A.; Rodrigues, D. R.; Dohi, T.; Kerber, N.; Seng, B.; Vafaee, M.; Everschor-Sitte, K.; Virnau, P.; Kläui, M. Skyrmion Pinning Energetics in Thin Film Systems. *Nat. Commun.* **2022**, *13*, 3144.
(65) Göbel, B.; Henk, J.; Mertig, I. Forming Individual Magnetic Biskyrmions by Merging Two Skyrmions in a Centrosymmetric Nanodisk. *Sci. Rep* **2019**, *9*, 9521.
(66) Ajejas, F.; Sassi, Y.; Legrand, W.; Collin, S.; Peña Garcia, J.; Thiaville, A.; Pizzini, S.; Reyren, N.; Cros, V.; Fert, A. Interfacial Potential Gradient Modulates Dzyaloshinskii-Moriya Interaction in Pt/Co/Metal Multilayers. *Phys. Rev. Materials* **2022**, *6* (7), L071401.
(67) Chen, G. *Skyrmion Hall Effect. Nature Phys.* **2017**, *13*, 112−113.
(68) Vélez, S.; Ruiz-Gómez, S.; Schaab, J.; Gradauskaite, E.; Wörnle, M. S.; Welter, P.; Jacot, B. J.; Degen, C. L.; Trassin, M.; Fiebig, M.;

https://doi.org/10.1021/acsnano.4c10145
ACS Nano 2024, 18, 31261−31273

Gambardella, P. Current-Driven Dynamics and Ratchet Effect of Skyrmion Bubbles in a Ferrimagnetic Insulator. *Nat. Nanotechnol.* **2022**, *17*, 834−841.
(69) Vansteenkiste, A.; Leliaert, J.; Dvornik, M.; Helsen, M.; Garcia-Sanchez, F.; Van Waeyenberge, B. The Design and Verification of MuMax3. *AIP Adv.* **2014**, *4*, 107133.

https://doi.org/10.1021/acsnano.4c10145
ACS Nano 2024, 18, 31261−31273